Nanoscale electronic inhomogeneity in ZrN$_x$ thin films growth by reactive sputtering at room temperature

N. Haberkorn[1,2] · J. Basbus[1,3] · S. Suárez[1,2] · M. Sirena[1,2]

Abstract

We report on the structural and electrical properties of nanocrystalline zirconium nitride films grown by reactive sputtering on Si (100) substrates at room temperature. The samples were grown with a N$_2$/Ar mixture varying the N$_2$ concentration between 8 and 60% of the total atmosphere. The films are nanocrystalline with the coexistence of conducting and insulator phases. The electrical resistivity evolves from ZrN with a metallic state to an insulating rich nitrogen phase, passing through a semiconductor-like behavior as N$_2$ in the mixture increases. A variable-range-hopping regime describes the temperature dependence of the resistivity for mixtures between 30 and 40%. Reactive mixtures of 50 and 60% of N$_2$ give more insulator films. Beyond these macroscopic properties, the films display inhomogeneity electrical properties at the nanoscale with coexistence regions of different conductivity. The inhomogeneities reduce as nitrogen stoichiometry increases and the films become more insulators. Our results are relevant for applications including conducting electrodes and insulator barriers in tunneling devices.

1 Introduction

The synthesis of thin films at low temperatures is of relevance for applications that include metastable properties in disordered materials [1–3] and for the development of flexible electronics on polymeric substrates [4–7]. Metal nitrides are attractive candidates for the development of devices based on different electrical behavior, corrosion resistance, hardness, and great surface activity [8–11]. For instance, zirconium nitrides are interesting for several technological applications due to tunable electronic properties (such as semiconducting, metallic, and insulator properties) [12–16] and great catalytic activity [17]. Zirconium nitride can crystallize in different crystal structures including ZrN (cubic) [18], Zr$_2$N (tetragonal) [19], c-Zr$_3$N$_4$ (cubic spinel) [20] and o-Zr$_3$N$_4$ (orthorhombic structure) [21]. ZrN displays a metallic behavior, and the c-Zr$_3$N$_4$ and o-Zr$_3$N$_4$ are insulating [14]. Nanocrystalline ZrN$_x$ thin films are usually prepared at low temperatures by reactive sputtering [22–27]. The reactive gas mixture modifies the nitrogen stoichiometry and the microstructure. As nitrogen content increases, the films become more amorphous, semi-transparent, and electrically resistive [20, 22, 24]. These changes may be related to the disorder generated by interstitial nitrogen, crystalline structure, and possible phase coexistence. The presence of disorder and coexistence of metallic/insulator regions may affect the performance of the samples and hinder some applications that require electrical homogeneity. Indeed, the electrical behavior in temperature and the homogeneity at the nanoscale are of technological relevance for its application as barriers and metallic electrodes in non-volatile memory devices [13] and Josephson junctions [14].

In this work, we analyze the influence of the reactive gas mixture on the structural and electrical properties of zirconium nitride thin films grown at room temperature by

✉ N. Haberkorn
nhaberk@cab.cnea.gov.ar

1   Centro Atómico Bariloche, Comisión Nacional de Energía Atómica and Consejo Nacional de Investigaciones Científicas y Técnicas, Av. Bustillo 9500, 8400 San Carlos de Bariloche, Argentina

2   Instituto Balseiro, Universidad Nacional de Cuyo and Comisión Nacional de Energía Atómica, Av. Bustillo 9500, 8400 San Carlos de Bariloche, Argentina

3   Istituto di Chimica della Materia Condensata e di Tecnologie per l'Energia, CNR, c/o DICCA-UNIGE, Via all'Opera Pia 15, 16145 Genoa, Italy

reactive sputtering on Si (100) substrates. The objective of the investigation is to find a correlation between stoichiometry and microstructure on the macroscopic and microscopic electrical properties of the system. Films were grown under an atmosphere with different nitrogen concentrations. The crystalline structure and chemical composition of the films is analyzed by X-ray diffraction (XRD) and Rutherford Backscattering Spectroscopy (RBS), respectively. The film morphology and homogeneity of the resistance at the nanoscale were evaluated using atomic force microscopy (AFM) and conductive AFM (CAFM), respectively. The electrical behavior was determined on the basis of the temperature dependence of the resistivity.

2 Experimental

ZrN_x films were deposited on Si (100) wafers by DC sputtering in an Ar/N_2 mixture without any intentional heating of the substrate. The films were grown using a power of 50 watts with a 99.99% purity Zr target (diameter: 0.038 m). During the deposition, the substrates were positioned directly over the targets at ~0.055 m. The base pressure was $\approx 6.7 \times 10^{-5}$ Pa. The total pressure during the deposition of the films was kept constant at 0.67 Pa. The N_2 partial pressure varies from 8 to 60% (controlling directly the Ar/N_2 pressure ratio). Ultra-high-purity Ar (99.999%) and N_2 (99.999%) were used as gas sources. The sputtering time was 30 min. Wherever used, the notation [ZrNX] corresponds to a zirconium nitride film with X nitrogen (%) mixture.

XRD patterns were collected at room temperature in air by a Panalytical Empyrean equipment with CuK_α radiation, graphite monochromator, operated at 40 kV and 30 mA. The structural analysis was performed based on Θ–2Θ scans with an angular step of 0.013°. The thicknesses of films were measured using their cross-sections by scanning electron microscopy (SEM), where the images were obtained by ZEISS Crossbeam 340 microscope operated at 2 keV and equipped with Energy Dispersive Spectroscopy (EDS) detectors for elementary analysis. The chemical composition of the films was analyzed by RBS with a TANDEM accelerator using a 2 MeV $^4He^{2+}$ ion beam. The topology of the films was characterized by AFM images in a Dimension 3100©Brucker microscope (contact mode). In addition, CAFM measurements were performed using diamond-doped conductive tips. Current–voltage (IV) curves were obtained using the ramp mode. The minimum detectable current in the CAFM used was 1 pA, and the maximum was 1000 nA, under a bias voltage ranging from 0.01 to 12 V. The electrical transport measurements for films growth N_2 gas mixtures up to 40% were performed using the standard four-terminal
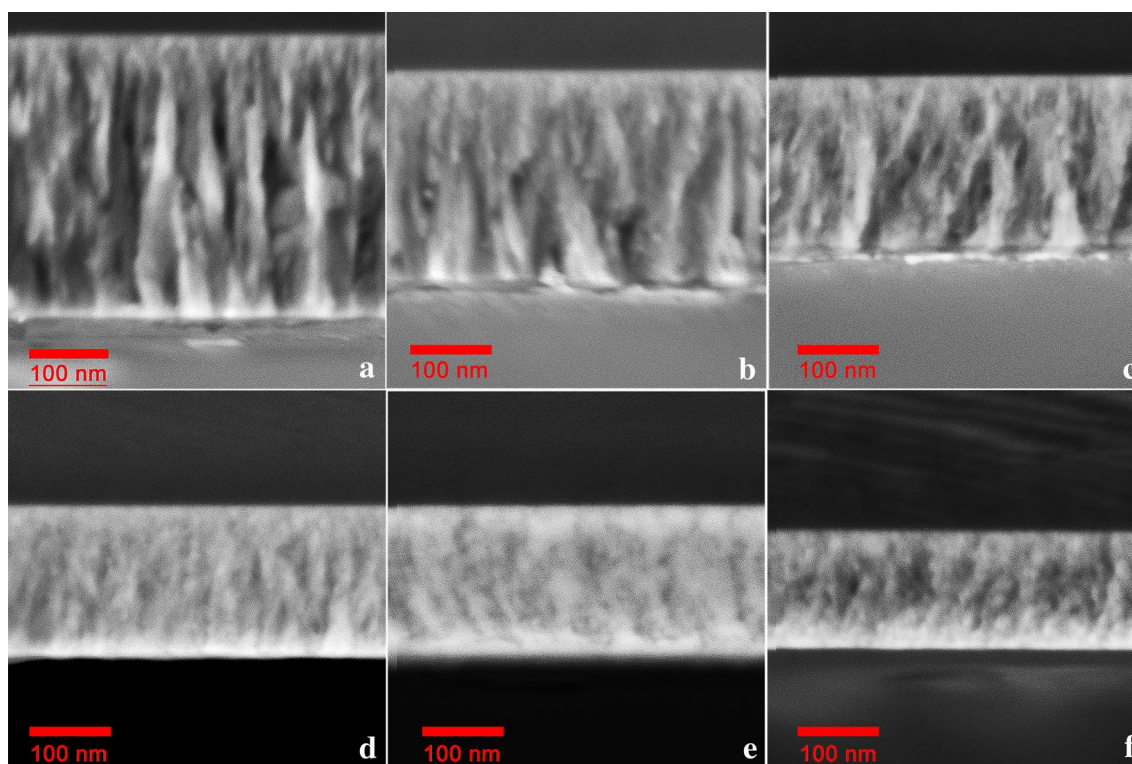
Fig. 1 Cross-sectional SEM images of $ZriN_x$ thin films. **a** [ZrN8]; **b** [ZrN18]; **c** [ZrN22]; **d** [ZrN30]; **e** [ZrN40]; **f** [ZrN60]
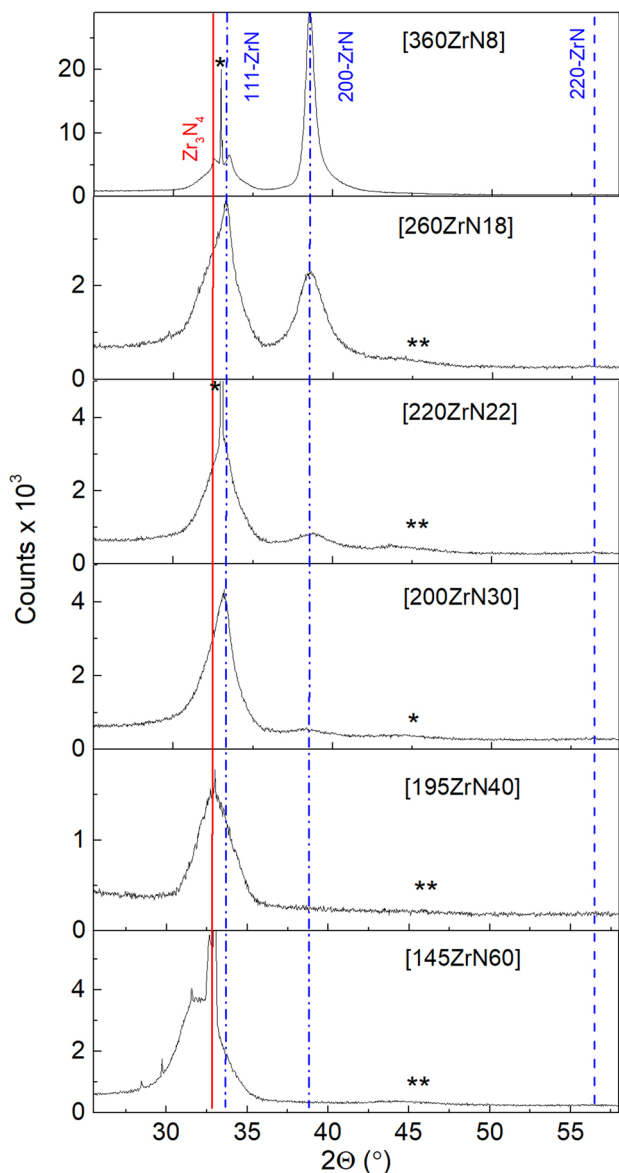
Fig. 2 XRD patterns for ZrN$_x$ thin films growth in different Ar/N$_2$ mixtures. The line for Zr$_3$N$_4$ corresponds an overlapping of the reflections (320), (201), (040) and (121). (*) Si (200). (**) Unidentified. The samples are indicated as [tZrNX], with t in nm

transport technique. A two-point technique with an electrometer was used to measure the resistivity in thin film growth using gas mixtures with 50 and 60% N$_2$.

3 Results and discussion

Figure 1 shows typical SEM cross-sectional images for films growth using different nitrogen concentrations. The films display smooth surfaces and their thickness (t) and microstructure change with the reactive atmosphere. For low nitrogen concentration, the films display a microstructure with columnar grains. The growth mechanism changes with the increment of nitrogen, and the columnar grains tend to disappear. Moreover, the growth rate change with the reactive atmosphere, decreasing from $\approx$12 to $\approx$5 nm / min as nitrogen in the gas mixture increases from 8 to 60%. The thicknesses obtained from the images are 360 nm for [ZrN8], 260 nm for [ZrN18], 220 nm for [ZrN22], 200 nm for [ZrN30], 196 nm for [ZrN40] and 145 nm for [ZrN60], corresponding to panels (a) to (f), respectively. Table 1 summarizes the film's thickness and other geometrical and electrical parameters.

Figure 2 shows the XRD patterns for films deposited in different reactive gas mixtures. The patterns display Bragg reflections related to the cubic ZrN (pdf card 03–065-9417). The film growth in a mixture with 8% N$_2$ shows the (111)$_{ZrN}$ and (200)$_{ZrN}$. The lattice parameter obtained from the peaks corresponds to $a = 0.465$ (1) nm, which is slightly higher than the tabulated for the stoichiometric compounds (0.457 nm). As the N$_2$ increases in the reactive gas mixture, the (200)$_{ZrN}$ reflection progressively decreases to disappear for gas mixtures higher than 40% N$_2$. A feature that emerges in the patterns is the presence of an asymmetric peak at 2Θ $\approx$33°, as evidence for [ZrN18]. This reflection systematically increases with the N$_2$ content, and it is the unique reflection for N$_2$ above 40%. Two different ways may analyze the nature of this peak. The first is related to cubic ZrN regions with different nitrogen stoichiometry and disorder. Indeed, in other systems such as Mo$_2$N, the excess of nitrogen in thin films modified the microstructure, producing a shift toward smaller 2Θ compared to stoichiometric ones [28]. On the other hand, at 2Θ $\approx$33°, the orthorhombic Zr$_3$N$_4$ (pdf card 01-087-0843) displays the reflections (320), (201), (040) and (121). However, considering the high structural disorder of the samples, the presence of Zr$_3$N$_4$ is unclear. Regarding cubic ZrN, the reduction of (200)$_{ZrN}$ increasing nitrogen suggests higher disorder due to large amount of interstitial nitrogen. Indeed, applying the Scherrer equation in the (200)$_{ZrN}$ reflection for a rough estimation and comparative purposes, where the crystallite size perpendicular to the plane reduces from 130 nm for [ZrN8], 50 nm for [ZrN18], and 36 nm [ZrN22]. The progressive reduction in the grain size average for the (200)$_{ZrN}$ reflection agrees with the systematic change in the growth mechanism evolving from a columnar structure to a granular one. The films with gas mixtures between 40 and 60% N$_2$ display a broad peak 2Θ $\approx$33°, a signature of disorder and nanometric grains. To verify an agreement between structural and chemical composition changes, we measured the Zr/N atomic ratio using RBS. The results show the following variations: 0.89 (0.05) for 8% N$_2$, 0.92 (0.05) for 18% N$_2$, 1.00 (0.05) for 22% N$_2$, 0.70 (0.05) for 30%, and 0.70 (0.05) for 40% N$_2$. The evolution in nitrogen
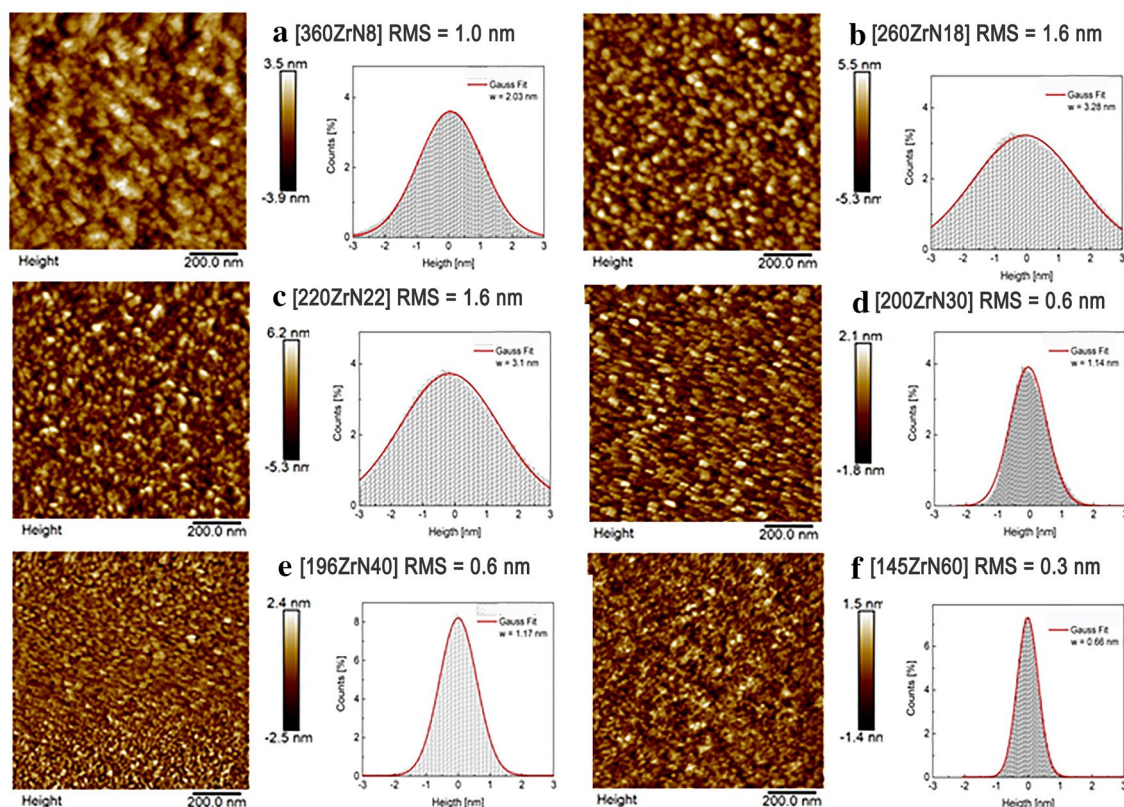
Fig. 3 AFM images with their RMS and roughness histograms of ZrN$_x$ thin films. The samples are indicated as [*t*ZrNX], with *t* in nm
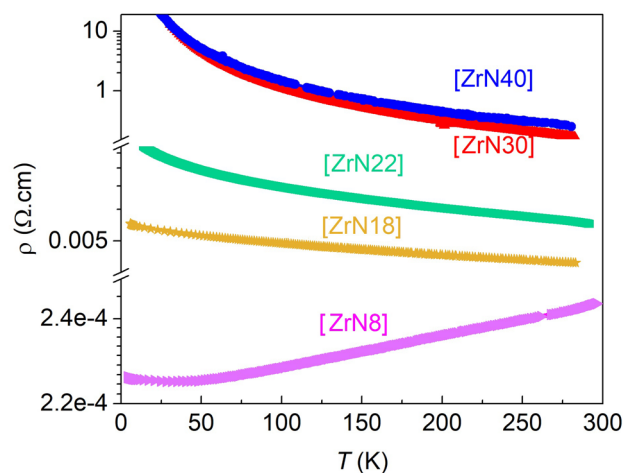

Fig. 4 Temperature dependence of the resistivity for ZrN$_x$ films grown using different reactive gas mixtures

stoichiometry relates to the changes in the microstructure of the films discussed above.

The influence of the reactive gas mixture on the surface morphology was analyzed using AFM images. Figure 3 shows typical AFM images (1×1 µm^2) and the respective histograms of peak height profile. The samples display flat surfaces, root-mean-square (RMS) roughness and the peak to valley height changes as nitrogen in the reactive mixture increases. The histograms seem to be Gaussian with no features of bimodal distribution. RMS roughness increases from N$_2$ 8 to 18% (1.0 to 1.6 nm), then it is stable for 18 and 22% (1.6 nm), and then it decreases from 1.6 to 0.3. The latter agrees with the reduction in the grain size and the suppression of the columnar structure originated by (200)$_{ZrN}$ texture.

The electrical behavior in the ZrN$_x$ films was determined from resistivity (ρ) versus temperature (*T*) measurements. Figure 4 shows a summary of the measurements for temperatures between 3 K and room temperature. The results show a gradual evolution from metallic to insulator behavior as the nitrogen in the mixture increases. [ZrN8] displays a metallic behavior with a residual resistivity ratio ($R^{300 K} / R^{10 K}$) of ≈1.1, which is a signature of high disorder as evidence contrasting the data with thin films grown at high temperatures [29]. Moreover, the disorder and grain size increase the resistivity at room temperature of ≈240 µΩ.cm, being much higher than the 12 µΩ.cm reported for epitaxial films [30]. The modification of the reactive gas mixture has a tremendous impact on the absolute values of resistivity and on its temperature behavior. Results indicate that the metallic behavior disappears for gas mixtures higher than 8% N$_2$.
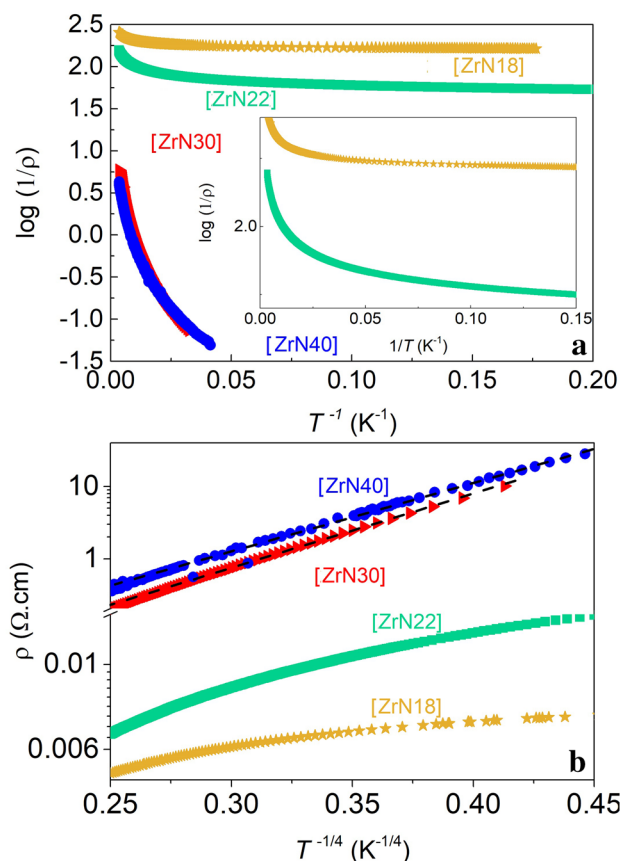
Fig. 5 **a** Plot of log (1/ρ) vs (1/T) for [ZrN18], [ZrN22], [ZrN30] and [ZrN40]. Inset: zoom of the data for [ZrN18], [ZrN22]. **b** Plot of log ρ vs $T^{-1/4}$ for the same films that panel (**a**). The straight dotted lines are the least-squares fits considering the VRH conduction law according to the Eq. 2

Results indicate that the metallic behavior disappears for gas mixtures higher than 8% N$_2$. As nitrogen increases, the films evolve to a semiconductor behavior with a systematic increment in the resistivity at room temperature as nitrogen in the gas mixture increases. The resistivity values at room temperature display an abrupt jump at mixtures between 22 (0.009 Ω.cm) and 30% (0.17 Ω.cm), increasing to 0.3 Ω.cm for 40% N$_2$. The resistivity for thin films growth at richer N$_2$ gas mixtures (more insulators) was measured in a two-point configuration from voltage-current curves. The value at room temperature from (V-I) curves for 50% N$_2$ is 10 Ω.cm. On the other hand, the V-I curve for 60% shows a non-Ohmic behavior (not shown). This behavior is usually observed in tunnel junctions and Schottky barriers and is outside the manuscript's scope [31, 32].

Following, the semiconductor behavior will be analyzed in more detail for [ZrN18], [ZrN22]. [ZrN30], and [ZrN40]. The increment in the resistivity of the films can be explained by the decrease in the grain size and the changes in the microstructure of the films. In general, the changes

in the microstructure of the films should induce changes in the transport mechanisms. It is important to mention that as the ZrN phase reduces and nitrogen content increases, and the films become more homogenous at the nanoscale. Figure 5a shows log (σ) vs (1/T) (σ being the conductivity) for the different films. For thermal activation conduction, the Arrhenius equation predicts:

$$\sigma(T) = \sigma_0 \exp\left[-\left(\frac{Ea}{kT}\right)\right], \tag{1}$$

where σ_0 is a pre-exponential factor, E_a is the activation energy, and is Boltzmann's constant [33]. The high-temperature conduction process in semiconductors usually comes from the electrons hopping from the donor levels to the valence band to acceptor levels. Our data in the different samples do not display a region in which (even at high temperatures) a linear region is identified and indicates the existence of a different or a combination of conduction mechanisms. The temperature dependence of the resistivity in disordered systems generally takes the form:

$$\rho \approx \rho_0 \exp\left[-\left(\frac{T_0}{T}\right)^p\right], \tag{2}$$

where ρ_0 is a prefactor, T_0 is a characteristic temperature and the exponent p depends on the shape of the density of states at the Fermi level (FL) [33]. For Mott variable-range-hopping (VRH), p can be ¼ (3D systems) or 1/3 (2D systems). Figure 5b shows ρ versus $T^{-1/4}$ in logarithm scale for the different films. The results show that for [ZrN30] and [ZrN40], a linear behavior is observed, whereas no agreement appears for [ZrN18] and [ZrN22]. The different behavior may be related to the fact that films grown with N$_2$ mixtures of 18 and 22% display an important fraction of the metallic ZrN phase and the electrical transport is not through a unique mechanism. The T_0 values obtained from the slopes for [ZrN30] and [ZrN40] are ≈10,000 and ≈139,000 K, respectively. These values are in the range of the reported for semiconducting ZnO [34] and smaller than those presented for ceramics such as CaCu$_3$Ti$_4$O$_{12}$ [35] and Cu-doped BaTiO$_3$ [36]. Using the values of T_0, it is possible to estimate the hopping energy $E_h(T)$ for a given temperature T [37]:

$$E_h(T) = \frac{1}{4} k_B T^{\frac{3}{4}} T_0^{\frac{1}{4}}. \tag{3}$$

The E$_h$ (5 K) goes from 0.27 to 1.4 meV when the nitrogen in the mixture is increased from 30 to 40%, which are values in the range of the reported for semiconducting ZnO [34].

To verify the role of the phase coexistence on the electrical properties at the nanoscale, the surface conductivity of
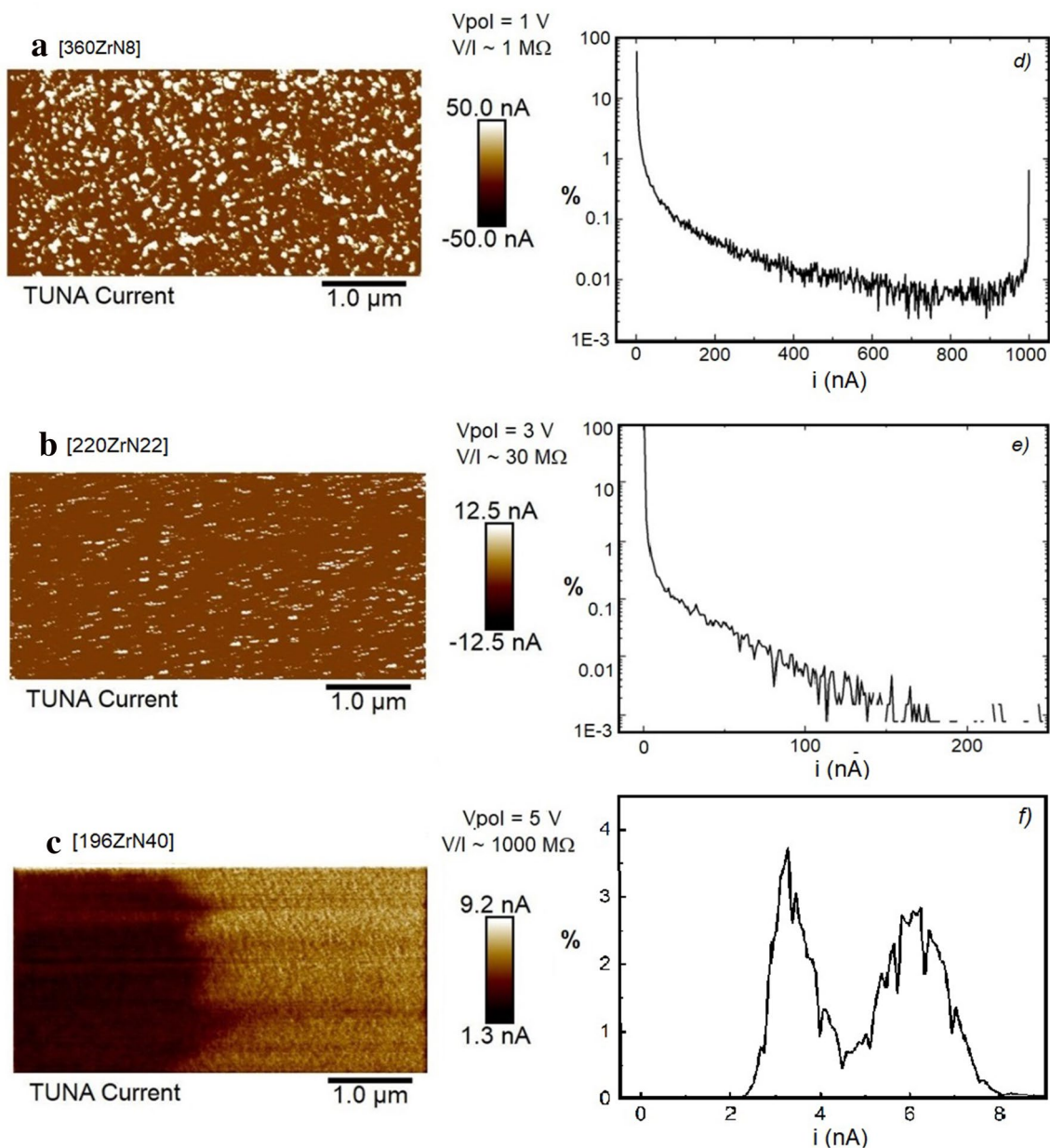
Fig. 6 Left Typical Conductive AFM images of ZrN_x films deposited in different reactive gas atmospheres and (right) their corresponding current distribution. Current bar was extended for a clear visualization in the color scale. The samples are indicated as [tZrNX], with t in nm

Table 1 Deposition parameters and main characteristics of ZrN_x thin films

$N_2/(N_2 + Ar)$	Deposition rate (nm/min)	Thickness (nm)	Zr/N at. %	RMS (nm)	Electrical behavior	$\rho^{298 K}$ (Ω.cm)
8	12	360	0.89 (0.05)	1.0	Metallic	0.00024
18	8.6	260	0.92 (0.05)	1.6	Semiconducting	0.004
22	7.3	220	1.00 (0.05)	1.6	Semiconducting	0.006
30	6.6	200	0.70 (0.05)	0.6	Semiconducting	0.17
40	6.5	196	0.67 (0.05)	0.6	Semiconducting	0.3
60	4.8	145	–	0.3	Non-Ohmic behavior	–

the samples was studied by CAFM at room temperature. Figure 6a–f shows the typical CAFM images and their current distribution of ZrN$_x$ samples with different nitrogen concentrations. Samples with low N concentration present a high mean conductivity (∼ 1MΩ) with a wide current distribution. High conductance areas of around 100 nm can be seen in the image (Fig. 6a and d). As the nitrogen concentration increases, the sample becomes more insulating (Fig. 6c–f). The current distribution shifts to lower currents and the size, density, and conductivity of the conducting areas decrease. The size of typical "high" conductive areas is below 50 nm, being of the same order that the columnar structure observed in Fig. 1. The sample with the highest nitrogen concentration is insulating (V/I ∼ 1000 MΩ) (Fig. 6c and f). Nevertheless, the homogeneity of the sample increases with increasing nitrogen concentration, showing for this sample a narrow Gaussian type current distribution. It should be noticed that the image and the current distribution of this sample present two different conducting areas (two Gaussian type current distributions are observed, Fig. 6f). The origin of this effect is probably a small experimental artifact, such as different pressures during the beginning and the end of the scan. The tip/sample forces can modify the contact area changing the effective conductance. The narrow current distribution of the sample makes this effect noticeable.

The results show that the microstructure of ZrN$_x$ thin films changes with the nitrogen content. We observe that films with mostly metallic ZrN phase display a columnar growth, which is in agreement with previous results [38]. Moreover, the resistivity of the films evolves as is expected for an increment in the nitrogen stoichiometry [22]. The results show that the conductivity of the films varies at the nanoscale, being more homogeneous as the films become more insulators. The inhomogeneities may be related to phase coexistence of metallic and insulator phases. Finally, it is important to note that for reactive gas mixtures between 30 and 40% of nitrogen, the films become more homogenous at the nanoscale and display semiconductor-like behavior with electrical properties dominated by VRH, which is in agreement with the expectations for disordered semiconducting systems. The possibility to tune electrical properties through phase separation may be of relevance for catalytic applications. On the other hand, semiconducting and insulator layers with homogeneous electrical properties are of relevance for tunneling devices.

4 Conclusions

We analyzed the influence of the chemical composition on the electronic properties of zirconium nitride thin films grown by reactive sputtering on Si (100) substrates at room temperature. The crystalline structure and electrical properties of the films are affected by the composition of the reactive gas mixture. The films display a resistivity that evolves from metallic to insulator, crossing through a semiconductor-like behavior as the nitrogen in the gas mixture increases from 8 to 60%. The semiconductor-like behavior agrees with phase separation at the nanoscale with insulator and metallic regions, indicating that the disorder plays a role in the electrical transport of the samples. The electrical properties become more homogenous as nitrogen increases and metallic ZrN reduces. The temperature dependence of the resistivity for films growth using nitrogen concentrations of 30 and 40% is described by VRH for 3D systems, which agrees with the expectations for disordered semiconductors. Finally, the films become more insulators for gas mixtures with 50 and 60%. Our results shed light on some limitations in the potential application of ZrN$_x$ thin films in electronic devices developed at room temperature.

References

1. A. Banerjee, L.J. Baker, A. Doye, M. Nord, R.M. Heath, K. Erotokritou, D. Bosworth, Z.H. Barber, I. MacLaren, R.H. Hadfield, Characterisation of amorphous molybdenum silicide (MoSi) superconducting thin films and nanowires. Supercond. Sci. Technol. **30**, 084010 (2017). https://doi.org/10.1088/1361-6668/aa76d8
2. C.M. Zgrabik, LHu. Evelyn, Optimization of sputtered titanium nitride as a tunable metal for plasmonic applications. Opt. Mater. Exp. **5**, 2786–2797 (2015). https://doi.org/10.1364/OME.5.002786
3. J.-S. Lee, J. Cho, C.-Y. You, Growth and characterization of α and β-phase tungsten films on various substrates. J. Vac. Sci. Technol. **34**, 021502 (2016). https://doi.org/10.1116/1.4936261
4. M.J. Twu, A.H. Chiou, C.C. Hu, C.Y. Hsu, C.G. Kuo, Properties of TiO2 films deposited on flexible substrates using direct current magnetron sputtering and using high power impulse magnetron sputtering. Polym. Degrad. Stab. **117**, 1–7 (2015). https://doi.org/10.1016/j.polymdegradstab.2015.03.010
5. Z. Rui, H. Zhenxuan, J. Xiangquan, Du. Jie Yang, Z.H. Bo, Yu. Shi, Deposition of molybdenum thin films on flexible polymer substrates by radio frequency magnetron sputtering. J. Nanosci. Nanotechnol. **16**, 8154–8159 (2016). https://doi.org/10.1166/jnn.2016.12782
6. V. Gupta, B. Yelamanchili, S. Zou, T. Isaacs-Smith, J. Sellers, D. Tuckerman, M. Hamilton, Thin-Film Nb/polyimide superconducting stripline flexible cables. IEEE Trans. Appl. Supercond. **29**, 1501605 (2019). https://doi.org/10.1109/TASC.2019.2904203
7. S.V. Zaitsev, N.I. Cherkashina, V.I. Pavlenko, D.S. Prochorenkov, Formation and stability of W coating on a flexible polyimide substrate. Thin Solid Films **715**, 138424 (2020). https://doi.org/10.1016/j.tsf.2020.138424

8. D. Roman, J. Bernardi, C.L.G. de Amorim, F.S. de Souza, A. Spinelli, C. Giacomelli, C.A. Figueroa, I.J.R. Baumvol, R.L.O. Basso, Effect of deposition temperature on microstructure and corrosion resistance of ZrN thin films deposited by DC reactive magnetron sputtering. Mater. Chem. Phys. **130**, 147–153 (2011). https://doi.org/10.1016/j.matchemphys.2011.06.013

9. S. Ghosh, S.M. Jeong, S.R. Polaki, A review on metal nitrides/oxynitrides as an emerging supercapacitor electrode beyond oxide. Korean J. Chem. Eng. **35**, 1389–1408 (2018). https://doi.org/10.1007/s11814-018-0089-6

10. S.A. Rasaki, B. Zhang, K. Anbalgam, T. Thomas, M. Yang, Synthesis and application of nano-structured metal nitrides and carbides: a review. Prog. Sol. State Chem. **50**, 1–15 (2018). https://doi.org/10.1016/j.progsolidstchem.2018.05.001

11. Z.B. Qia, Z.T. Wu, H.F. Liang, D.F. Zhang, J.H. Wang, Z.C. Wanga, In situ and ex situ studies of microstructure evolution during high-temperature oxidation of ZrN hard coating. Scripta Mater. **97**, 9–12 (2015). https://doi.org/10.1016/j.scriptamat.2014.10.024

12. Y. Wang, F. Cao, M. Ding, D. Yang, Investigation of Zr–N thin films for use as diffusion barrier in Cu metallization. Microelectron. J. **38**, 910–914 (2007). https://doi.org/10.1016/j.mejo.2007.06.001

13. J. Westlinder, J. Malmström, G. Sjöblom, J. Olsson, Low-resistivity ZrNx metal gate in MOS devices. Sol. State Electron. **49**, 1410–1413 (2005). https://doi.org/10.1016/j.sse.2005.06.021

14. K. Schwarz, A.R. Williams, J.J. Cuomo, J.H.E. Harper, H.T.G. Hentzell, Zirconium nitride a new material for Josephson junctions. Phys. Rev B **32**, 8312 (1985). https://doi.org/10.1103/PhysRevB.32.8312

15. T. Yotsuya, M. Yoshitake, New type cryogenic thermometer using sputtered Zr-N films. Appl. Phys. Lett. **51**, 235 (1987). https://doi.org/10.1063/1.98459

16. S. Zhang, J. Wang, Wu. Rong, L. Liu, B.P.C. Liu, Structural and corrosion resistance properties of sputtered zirconium nitride thin films as electrode material for supercapacitor. J. Alloys Comp. **900**, 163506 (2022). https://doi.org/10.1016/j.jallcom.2021.163506

17. Y. Yuan, J. Wang, S. Adimi, H. Shen, T. Thomas, R. Ma, J.P. Attfield, M. Yang, Zirconium nitride catalysts surpass platinum for oxygen reduction. Nat. Mater. **19**, 282–286 (2020). https://doi.org/10.1038/s41563-019-0535-9

18. A. Ul-Hamid, The effect of deposition conditions on the properties of Zr-carbide, Zr-nitride and Zr-carbonitride coatings – a review. Mater. Adv. **1**, 988–1011 (2020). https://doi.org/10.1039/D0MA00232A

19. J.P. Dauchot, S. Edart, M. Wautelet, M. Hecq, Synthesis of zirconium nitride films monitored by in situ soft X-ray spectrometry. Vaccum **46**, 927–930 (1995). https://doi.org/10.1016/0042-207X(95)00074-7

20. A. Zerr, G. Miehe, R. Riedel, Synthesis of cubic zirconium and hafnium nitride having Th3P4 structure. Nat. Mater. **2**, 185–189 (2003). https://doi.org/10.1038/nmat836

21. M. Lerch, E. Fuglein, J. Wrba, Synthesis, crystal structure, and high temperature behavior of Zr3N4 Z. Anorg. Allg. Chem. **622**, 367–372 (1996). https://doi.org/10.1002/zaac.19966220227

22. H.M. Benia, M. Guemmaz, G. Schmerber, A. Mosser, J.-C. Parlebas, Investigations on non-stoichiometric zirconium nitrides. Appl. Surf. Scie **200**, 231–238 (2002). https://doi.org/10.1016/10.1016/S0169-4332(02)00925-X

23. R. Lamni, E. Martinez, S.G. Springer, R. Sanjines, P.E. Schmid, F. Levy, Optical and electronic properties of magnetron sputtered ZrNx thin films. Thin Solid Films **447–448**, 316–321 (2004). https://doi.org/10.1016/S0040-6090(03)01109-X

24. D.S. Yee, J.J. Cuomo, M.A. Frisch, D.P.E. Smith, Reactive radio frequency sputter deposition of higher nitrides of titanium, zirconium, and hafnium. J. Vacuum Scie Tech A **4**, 381 (1986). https://doi.org/10.1116/1.573933

25. M. Östling, S. Nygren, C.S. Petersson, H. Norström, R. Buchta, H.-O. Blom, S. Berg, A comparative study of the diffusion barrier properties of TiN and ZrN. Thin Solid Films **145**, 81–88 (1986). https://doi.org/10.1016/0040-6090(86)90254-3

26. C.-P. Liu, H.-G. Yang, Systematic study of the evolution of texture and electrical properties of ZrNx thin films by reactive DC magnetron sputtering. Thin Solid Films **444**, 111–119 (2003). https://doi.org/10.1016/S0040-6090(03)01191-X

27. N. Farkas et al., Characterization of zirconium nitride films sputter deposited with an extensive range of nitrogen flow rates. J. Vacuum Sci. Technol. A **26**, 297 (2008). https://doi.org/10.1116/1.2839856

28. N. Haberkorn, S. Bengio, S. Suárez, P.D. Pérez, M. Sirena, J. Guimpel, Effect of the nitrogen-argon gas mixtures on the superconductivity properties of reactively sputtered molybdenum nitride thin films. Mater. Lett **215**, 15–18 (2018). https://doi.org/10.1016/j.matlet.2017.12.045

29. A. Cassinese, M. Iavarone, R. Vaglio, M. Grimsditch, S. Uran, Transport properties of ZrN superconducting films. Phys. Rev B **62**, 13915 (2000). https://doi.org/10.1103/PhysRevB.62.13915

30. A.B. Mei, Physical properties of epitaxial ZrN/MgO(001) layers grown by reactive magnetron sputtering. J. Vacuum Sci. Technol. A **31**, 061516 (2013). https://doi.org/10.1116/1.4825349

31. J. Brillson, Y. Lu, ZnO Schottky barriers and Ohmic contacts. J. Appl. Phys. **109**, 121301 (2011). https://doi.org/10.1063/1.3581173

32. H. Kohlstedt, N.A. Pertsev, J.R. Contreras, R. Waser, Theoretical current–voltage characteristics of ferroelectric tunnel junctions. Phys. Rev. B **72**, 125341 (2005). https://doi.org/10.1103/PhysRevB.72.125341

33. I.S. Beloborodov, A.V. Lopatin, V.M. Vinokur, K.B. Efetov, Granular electronic systems. Rev. Mod. Phys. **79**, 469–518 (2007). https://doi.org/10.1103/RevModPhys.79.469

34. Y.-L. Huang, S.-P. Chiu, Z.-X. Zhu, Z.-Q. Li, J.-J. Lin, Variable-range-hopping conduction processes in oxygen deficient polycrystalline ZnO films. J. Appl. Phys. **107**, 063715 (2010). https://doi.org/10.1063/1.33573767

35. L. Zhang, Z.-J. Tang, Polaron relaxation and variable-range-hopping conductivity in the giant-dielectric-constant material CaCu3Ti4O12. Phys. Rev B **70**, 174306 (2004). https://doi.org/10.1103/PhysRevB.70.174306

36. C. Ang, Z. Jing, Yu. Zhi, Variable-range-hopping conduction and metal–insulator transition in Cu-doped BaTiO3. J. Phys. Condens. Mater **11**, 9703–9708 (1999). https://doi.org/10.1088/0953-8984/11/48/327

37. S. Ravi, M. Kar, Study of magneto-resistivity in La1-xAgxMnO3 compounds. Physica B: Cond. Matter **348**, 169–176 (2004). https://doi.org/10.1016/j.physb.2003.11.087

38. R. Mareus, C. Mastail, F. Anğay, N. Brunetière, G. Abadias, Study of columnar growth, texture development and wettability of reactively sputter-deposited TiN, ZrN and HfN thin films at glancing angle incidence. Surf. Coat. Technol. **399**, 126130 (2020). https://doi.org/10.1016/j.surfcoat.2020.126130